

# DEPROJECTING SERSIC PROFILES FOR ARBITRARY TRIAXIAL SHAPES: ROBUST MEASURES OF INTRINSIC AND PROJECTED GALAXY SIZES

GLENN VAN DE VEN<sup>1,3</sup> AND ARJEN VAN DER WEL<sup>2,3</sup>

*Draft version April 6, 2021*

## ABSTRACT

We present the analytical framework for converting projected light distributions with a Sérsic profile into three-dimensional light distributions for stellar systems of arbitrary triaxial shape. The main practical result is the definition of a simple yet robust measure of intrinsic galaxy size: the median radius  $r_{\text{med}}$ , defined as the radius of a sphere that contains 50% of the total luminosity or mass, that is, the median distance of a star to the galaxy center. We examine how  $r_{\text{med}}$  depends on projected size measurements as a function of Sérsic index and intrinsic axis ratios, and demonstrate its relative independence of these parameters. As an application we show that the projected semi-major axis length of the ellipse enclosing 50% of the light is an unbiased proxy for  $r_{\text{med}}$ , with small galaxy-to-galaxy scatter of  $\sim 10\%$  ( $1\sigma$ ), under the condition that the variation in triaxiality within the population is small. For galaxy populations with unknown or a large range in triaxiality an unbiased proxy for  $r_{\text{med}}$  is  $1.3 \times R_e$ , where  $R_e$  is the circularized half-light radius, with galaxy-to-galaxy scatter of 20–30% ( $1\sigma$ ). We also describe how inclinations can be estimated for individual galaxies based on the measured projected shape and prior knowledge of the intrinsic shape distribution of the corresponding galaxy population. We make the numerical implementation of our calculations available.

## 1. INTRODUCTION

The spatial distribution of stars in a galaxy encodes key information about its formation history, whether dissipative or dissipationless processes dominated and whether angular momentum has been retained or lost. The half-light radius is the simplest observational measure of stellar mass distribution. From an empirical perspective, this quantity has played a central role in defining the nature of galaxies through examining and interpreting their scaling relations (e.g., Kormendy 1977; Djorgovski & Davis 1987; Dressler et al. 1987) and tracking the build up of galaxies through cosmic time (e.g., Trujillo et al. 2004; van der Wel et al. 2014a). From a theoretical perspective, galaxy sizes have repeatedly revealed that essential physical elements are missing in galaxy formation models (e.g., Navarro & Steinmetz 2000), leading to the implementation of (astro)physical processes such as feedback.

Measurements of galaxy sizes as traced by stellar light have now reached a point where 0.1 dex accurate statements about two-dimensional (2D) projected galaxy sizes across cosmic time can be made with great precision (e.g., Mowla et al. 2019; van der Wel et al. 2014a). Currently, we are limited by the interpretation of the data, not its scarcity – almost a unicum in the field of galaxy evolution. One limiting factor is the missing link between the projected size (the half-light radius that we measure) and a physically more directly meaningful quantity such as the average or median distance of a star to the center of its galaxy. This conversion factor, from projected to

three-dimensional (3D) intrinsic size, can vary by large factors given the range of possible galaxy shapes and projections. As a result, comparisons with simulations have remained indirect and prone to systematic effects (e.g., Parsotan et al. 2021; Ludlow et al. 2019; Genel et al. 2018).

We note that we take the word *size* to mean the 2D projected or 3D intrinsic half-light radius (or, ideally, half-mass radius) that serves to quantify what we define as the mean radius of the galaxy. Other definitions of size adopt a fixed surface brightness or density threshold, aiming to quantify the *full extent* of the galaxy, which is a useful but qualitatively different quantity from the mean radius.

To our knowledge attempts at the deprojection of measured 2D light profiles so far have assumed spherical symmetry (e.g., Bezanson et al. 2009), simplifying the calculation, but failing to account for the fact that in reality most galaxies are far from spherical: even most early-type galaxies have an intrinsic short-to-long axis ratio of no more than  $\sim 0.3$  (e.g., Vincent & Ryden 2005), which more recently has been shown to be the case across cosmic time (e.g., Chang et al. 2013). In this paper we present the analytical framework and numerical implementation for the conversion of 2D light profiles to 3D light distributions for galaxies of arbitrary triaxial shape. Only with this machinery can we take full advantage of the available high-quality data and make accurate comparisons with theoretical predictions.

This paper is organised as follows: Section 2 describes how triaxial shapes project in 2D; Section 3 depicts the deprojection of Sérsic profiles; Section 4 introduces the definition and derivation of the median radius,  $r_{\text{med}}$ ; Section 5 outlines how to infer, in practice,  $r_{\text{med}}$  from projected size and shape measurements; Section 6 concludes with a brief description of implications of our findings for galaxy size estimates.

<sup>1</sup>Department of Astrophysics, University of Vienna, Türkenschanzstrasse 17, 1180 Vienna, Austria; glenn.vandeven@univie.ac.at

<sup>2</sup>Sterrenkundig Observatorium, Department of Physics and Astronomy, Ghent University, Belgium; arjen.vanderwel@ugent.be

<sup>3</sup>Max-Planck Institut für Astronomie, Königstuhl 17, D-69117, Heidelberg, Germany

## 2. ELLIPSOIDAL SHAPES

We consider intrinsic density distributions  $\rho(x, y, z) = \rho(m)$  that are constant on ellipsoids

$$m^2 = \frac{x^2}{a^2} + \frac{y^2}{b^2} + \frac{z^2}{c^2}, \quad (1)$$

with  $a \geq b \geq c$ . The major semi-axis length  $a$  is a scale parameter, whereas the intermediate-over-major ( $p \equiv b/a$ ) and minor-over-major ( $q \equiv c/a$ ) axis ratios determine the intrinsic shape. In the oblate or prolate axisymmetric limit we have  $a = b > c$  (pancake-shaped) or  $a > b = c$  (cigar-shaped), respectively, while in the spherical limit  $a = b = c$  (so then  $m = r/a$ ). Note that  $m$  is a dimensionless ellipsoidal radius.

We introduce a new Cartesian coordinate system  $(x'', y'', z'')$ , with  $x''$  and  $y''$  in the plane of the sky and the  $z''$ -axis along the line-of-sight. Choosing the  $x''$ -axis in the  $(x, y)$ -plane of the intrinsic coordinate system (cf. de Zeeuw & Franx 1989) and their Fig. 2), the transformation between both coordinate systems is known once two viewing angles, the polar angle  $\vartheta$  and azimuthal angle  $\varphi$ , are specified. The intrinsic  $z$ -axis projects onto the  $y''$ -axis; for an axisymmetric galaxy model the  $y''$ -axis aligns with the short axis of the projected density,<sup>4</sup> but for a triaxial galaxy model the  $y''$ -axis is misaligned by an angle  $\psi \in [-\pi/2, \pi/2]$  such that (cf. equation B9 of Franx 1988)

$$\tan 2\psi = \frac{T \sin 2\varphi \cos \vartheta}{\sin^2 \vartheta + T (\sin^2 \varphi \cos^2 \vartheta - \cos^2 \varphi)}, \quad (2)$$

where  $T$  is the triaxiality parameter defined as  $T = (a^2 - b^2)/(a^2 - c^2)$ . A rotation through  $\psi$  transforms the coordinate system  $(x'', y'', z'')$  to  $(x', y', z')$  such that the  $x'$  and  $y'$  axes are aligned with the major and minor axes of the projected density (respectively), while  $z' = z''$  is along the line-of-sight.

Projecting  $\rho(m)$  along the line-of-sight yields a surface density  $\Sigma(x', y') = \Sigma(m')$  that is constant on ellipses in the sky-plane,

$$\Sigma(m') = \int_{-\infty}^{\infty} \rho(m) dz' = \frac{abc}{a'b'} 2 \int_0^{\infty} \rho(m) m du, \quad (3)$$

where we have used  $z' = abc \sinh(u)/(a'b') + \text{constant}$ , and  $m = m' \cosh(u)$ . The sky-plane ellipse is given by

$$m'^2 = \frac{x'^2}{a'^2} + \frac{y'^2}{b'^2}. \quad (4)$$

The projected major and minor semi-axis lengths,  $a'$  and  $b'$ , depend on the intrinsic semi-axis lengths  $a$ ,  $b$ , and  $c$  and the viewing angles  $\vartheta$  and  $\varphi$  as follows:

$$a'^2 = \frac{2A^2}{B - \sqrt{B^2 - 4A^2}}, \quad b'^2 = \frac{2A^2}{B + \sqrt{B^2 - 4A^2}}, \quad (5)$$

<sup>4</sup> For an oblate galaxy, the alignment ( $\psi = 0$ ) follows directly from equation (2) since  $T = 0$ . For a prolate galaxy it is most easily seen by exchanging  $a$  and  $c$  ( $c > b = a$ ), so that the  $z$ -axis is again the symmetry axis (instead of the  $x$ -axis).

where  $A$  and  $B$  are defined as

$$\begin{aligned} A^2 &= a^2 b^2 \cos^2 \vartheta + (a^2 \sin^2 \varphi + b^2 \cos^2 \varphi) c^2 \sin^2 \vartheta, \quad (6) \\ B &= a^2 (\cos^2 \varphi \cos^2 \vartheta + \sin^2 \varphi) \\ &\quad + b^2 (\sin^2 \varphi \cos^2 \vartheta + \cos^2 \varphi) + c^2 \sin^2 \vartheta. \quad (7) \end{aligned}$$

It follows that  $A = a'b'$  is proportional to the area of the ellipse.

The flattening  $q' \equiv b'/a'$  of the projected ellipses actually depends on the viewing angles ( $\vartheta, \varphi$ ) and the intrinsic axis ratios ( $b/a, c/a$ ), and is independent of the scale length. Since the intrinsic and projected semi-major axis lengths are directly related via the left equation of (5), the scale length can be set by choosing either  $a$  or  $a'$ .

In what follows, we will describe the density and related quantities in terms of mass, including intrinsic mass density, surface mass density and enclosed mass. Without loss of generality, these quantities may also be expressed in terms of light, i.e., intrinsic luminosity density, surface brightness, and enclosed luminosity. However, mixing of mass and light quantities requires an additional conversion with the mass-to-light ratio which in general varies with galactic radius.

## 3. DEPROJECTED SÉRSIC DENSITY PROFILES

It has long been known that the stellar surface density profiles of early-type galaxies and of spiral galaxy bulges are well described by a Sérsic (1968) profile  $\Sigma(R) \propto \exp[-(R/R_e)^{1/n}]$ , with the effective radius  $R_e$  enclosing half of the total stellar mass. A key conceptual difference from cusped models is that the profile does not converge to a particular inner slope on small scales. Unfortunately, the deprojection of the Sérsic surface density profile cannot be expressed in common functions (for special functions see Baes & van Hese 2011), but is well approximated by the analytic density profile of Prugniel & Simien (1997)

$$\rho(m) = \frac{\rho_0}{m^{p_n}} \exp[-b_n m^{1/n}], \quad (8)$$

where the inner negative slope is given by

$$p_n = 1 - \frac{0.6097}{n} + \frac{0.05563}{n^2}. \quad (9)$$

The enclosed mass for the Prugniel-Simien model is

$$M(< m) = 4\pi abc \rho_0 n b_n^{(p_n-3)n} \gamma[(3-p_n)n, b_n m^{1/n}], \quad (10)$$

where  $\gamma[p; x]$  is the incomplete gamma function, which in the case of the total luminosity reduces to the complete gamma function  $\Gamma[p] = \gamma[p; \infty]$ .

The expression for the surface density is, to high accuracy, the Sérsic profile

$$\Sigma(m') = \Sigma_0 \exp[-b_n (m')^{1/n}]. \quad (11)$$

Given the enclosed projected mass

$$M'(< m') = 2\pi a'b'\Sigma_0 n b_n^{-2n} \gamma[2n, b_n (m')^{1/n}], \quad (12)$$

the requirement that the total intrinsic and projected mass have to be equal yields a normalisation

$$\Sigma_0 = \frac{abc}{a'b'} \rho_0 \frac{2\Gamma[(3-p_n)n]}{b_n^{(1-p_n)n} \Gamma[2n]}. \quad (13)$$

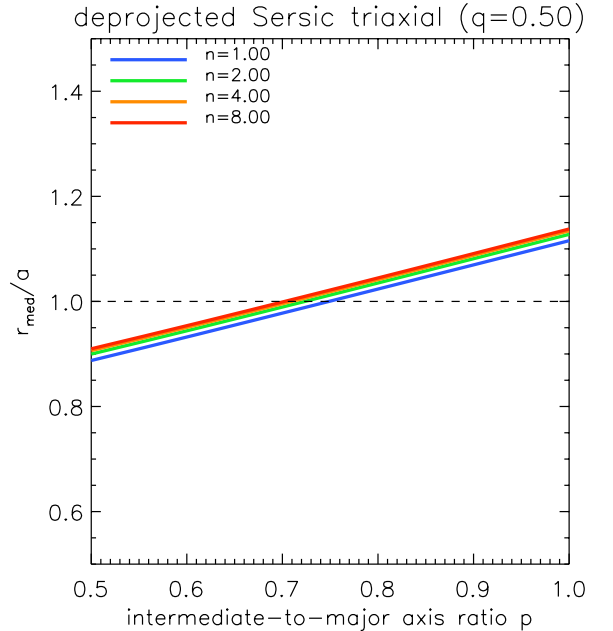
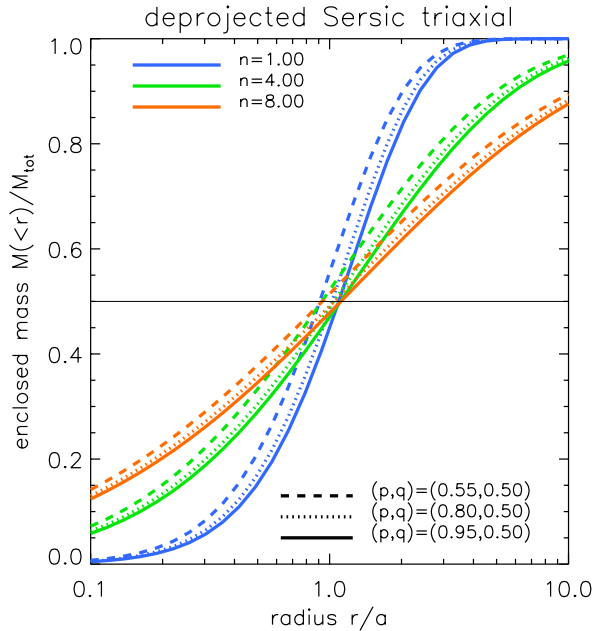
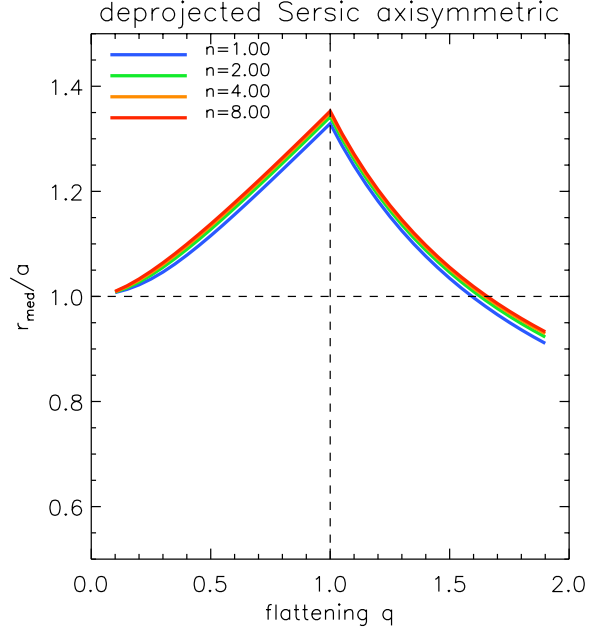
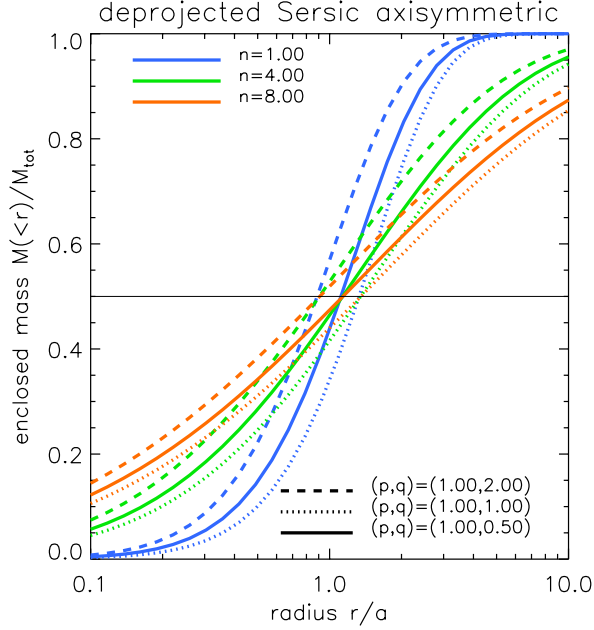


**Figure 1.** De-projected Sérsic profile. The enclosed mass  $M(<r)$  normalized by the total mass  $M_{\text{tot}}$ , within a spherical radius  $r$  normalized by the scale length  $a$ . As indicated, the colors represent different Sérsic index  $n$  and the line styles different intrinsic shapes given by the intrinsic axis ratios  $p = b/a$  and  $q = c/a$ . The *top* panel is for spheroidal shapes, either oblate axisymmetric ( $q < 1$ ) or prolate axisymmetric ( $q > 1$ ), and the *bottom* panel for fully triaxial shapes.

**Figure 2.** The median radius  $r_{\text{med}}$  of a de-projected Sérsic profile normalized by the scale length  $a$  when the enclosed mass is equal to half of the total mass (i.e., the intersections of the curves in Figure 1 with the horizontal line at 0.5). The *top* panel is for spheroidal shapes, either oblate axisymmetric ( $q < 1$ ) or prolate axisymmetric ( $q > 1$ ), and the *bottom* panel for fully triaxial shapes. In all cases,  $r_{\text{med}}/a$  depends on the intrinsic shape, but only mildly on the Sérsic index  $n$ .

The value of  $b_n$  depends on the index  $n$  and the choice for the scale length. The latter is commonly chosen to be the effective radius  $R_e$  in the stellar surface density profile, which contains half of the total stellar mass. We adopt a similar convention requiring that the ellipse  $m' = 1$  contains half of the projected mass. This choice results in the relation  $\Gamma[2n] = 2\gamma[2n, b_n]$ , which to high precision

can be approximated by (cf. Ciotti & Bertin 1999)

$$b_n = 2n - \frac{1}{3} + \frac{4}{405} \frac{1}{n} + \frac{46}{25515} \frac{1}{n^2}. \quad (14)$$

#### 4. MEDIAN RADIUS

We suggest as a robust measure for the size of a galaxy the median spherical radius. To infer this value numeri-

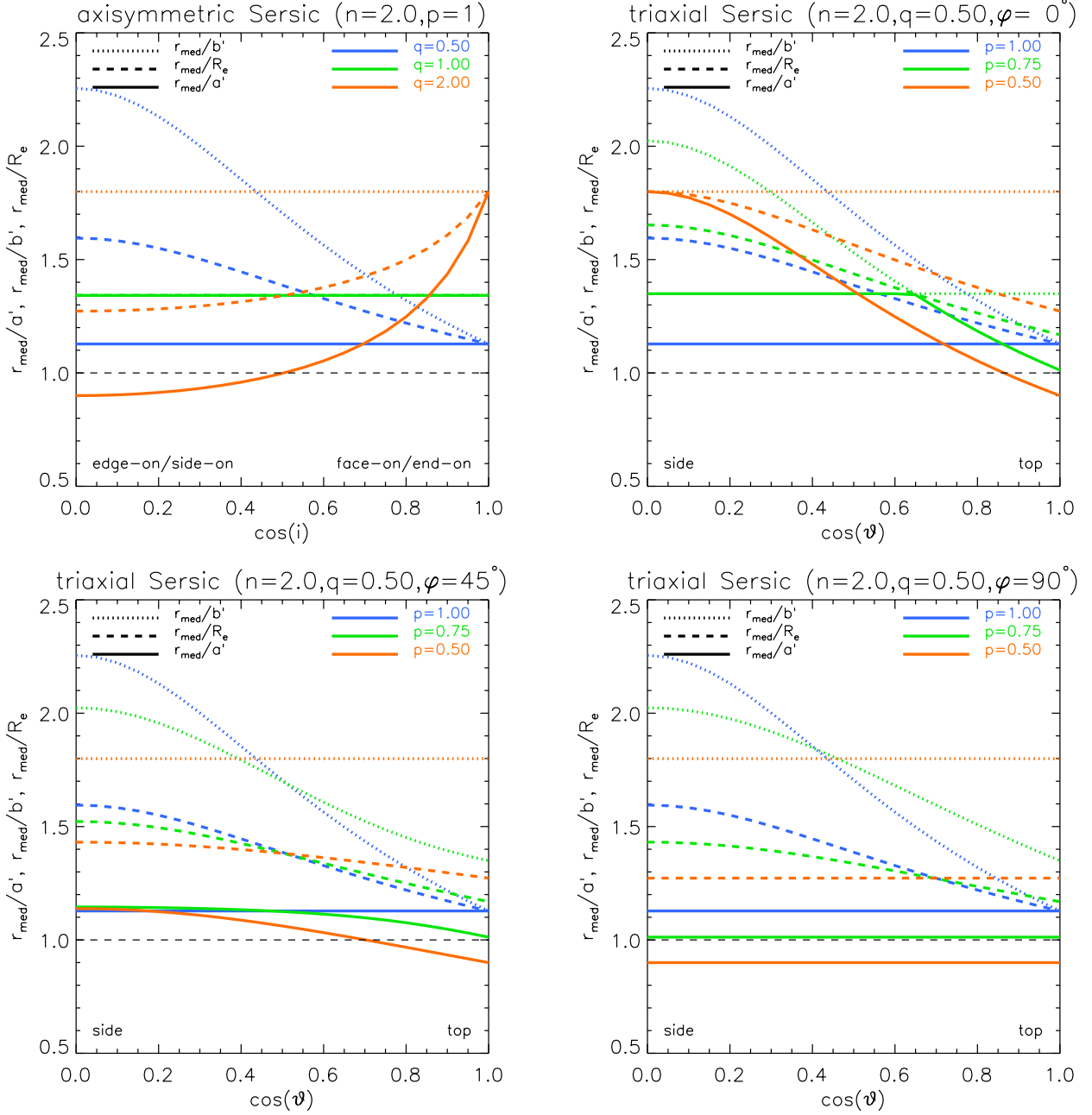


**Figure 3.** The median radius  $r_{\text{med}}$  of a deprojected Sérsic profile normalized by the projected semi-major axis length  $a'$  (solid curves) and semi-minor axis length  $b'$  (dotted curves), as well as effective radius  $R_e$  (dashed curves), as function of the polar viewing angle  $\vartheta$ . The *top-left* panel is for the axisymmetric case with inclination  $i$  ranging from  $\cos i = 0$  for edge-on (side-on) to  $\cos i = 1$  for face-on (end-on) in the oblate (prolate) axisymmetric case, with intrinsic flattening  $q < 1$  ( $q > 1$ ) indicated by the different colors. The *other three panels* are for the triaxial case, which in addition to the polar viewing angle  $\vartheta$ , also depends on the azimuthal viewing angle  $\varphi$  with values indicated above each panel. The intrinsic short-to-major axis ratio is fixed to  $q = 0.5$ , whereas the colors indicate different intrinsic intermediate-to-major axis ratios  $p$ .

cally we have to find the spherical radius which encloses half of the stellar mass. The mass enclosed within a spherical radius  $r$  follows from

$$M(< r) = \int_0^r \tilde{r}^2 d\tilde{r} \int_0^\pi \sin \theta d\theta \int_0^{2\pi} d\phi \rho[m(r, \theta, \phi)], \quad (15)$$

with ellipsoidal radius  $m(r, \theta, \phi) = (r/a) C_{pq}(\theta, \phi)$ , where we have defined

$$C_{pq}^2(\theta, \phi) = \sin^2 \theta \left( \cos^2 \phi + \frac{\sin^2 \phi}{p^2} \right) + \frac{\cos^2 \theta}{q^2}, \quad (16)$$

and as before  $p = b/a$  and  $q = c/a$ . Substituting the deprojected Sérsic density of equation (8), we see that the integral over radius is an incomplete gamma function,

so that

$$M(< r) = 4\pi a^3 \rho_0 n b_n^{(p_n-3)n} \int_0^1 d \cos \theta \int_0^1 d(\phi/2\pi) \\ \times \gamma[(3-p_n)n, b_n (C_{pq} r/a)^{1/n}] C_{pq}^{-3}. \quad (17)$$

With the total stellar mass given by equation (10) for  $m \rightarrow \infty$ , the median radius normalized by the scale length  $r_{\text{med}}/a$ , follows upon numerically solving

$$2pq \gamma[(3-p_n)n] = \int_0^1 d \cos \theta \int_0^1 d(\phi/2\pi) \\ \times \gamma[(3-p_n)n, b_n (C_{pq} r_{\text{med}}/a)^{1/n}] C_{pq}^{-3}. \quad (18)$$

When  $p = 1$  in oblate axisymmetry the integral over  $\phi$  can be discarded. In case of prolate axisymmetry, it is easiest to exchange  $a$  and  $c$ , so that again  $p = 1$  and the integral over  $\phi$  can be discarded, whereas  $q > 1$  and the resulting  $r_{\text{med}}/c$  has to be divided by  $q$  to obtain  $r_{\text{med}}/a$ .

As can be seen from Figures 1 and 2, the resulting  $r_{\text{med}}/a$  depends on the intrinsic axis ratios  $p$  and  $q$ , but very little on Sérsic index  $n$ . This implies that the median radius is robust against measurement errors in  $n$ .

In practice we cannot measure the intrinsic scale length  $a$ , but instead we measure the projected semi-major axis length  $a'$  and semi-minor axis length  $b'$ . Using the relations (5), we infer the ratio of the median radius to these projected length scales. Figure 3 shows the resulting  $r_{\text{med}}/a'$  (solid curves),  $r_{\text{med}}/b'$  (dotted curves), and  $r_{\text{med}}/R_e$  (dashed curves) with the adopted definition  $R_e^2 = a'b'$ , as function of the polar viewing angle  $\vartheta$ .

In the axisymmetric case (top-left panel), the latter polar angle is the inclination  $i$ , ranging from  $\cos i = 0$  for edge-on (side-on) to  $\cos i = 1$  for face-on (end-on) in the oblate (prolate) axisymmetric case, with intrinsic flattening  $q < 1$  ( $q > 1$ ) indicated by the different colors.

In the triaxial case, the polar angle  $\vartheta$  ranges from viewing the short axis from the side ( $\cos \vartheta = 0$ ) to from the top ( $\cos \vartheta = 1$ ). In addition, the projection depends on the azimuthal viewing angle  $\varphi$ , which ranges from viewing from along the long axis ( $\varphi = 0^\circ$ , top-right panel), intermediate between long and short axis ( $\varphi = 45^\circ$ , bottom-left panel) to along the intermediate axis ( $\varphi = 90^\circ$ , bottom-right panel). The intrinsic short-to-major axis ratio is fixed to  $q = 0.5$ , whereas the colors indicate different intrinsic intermediate-to-major axis ratios  $p$ .

In all four panels the blue curves correspond to the same oblate axisymmetric case ( $p = 1, q = 0.5$ ), which is independent of the azimuthal angle  $\varphi$ . Even though the red curves also correspond to the prolate case with the same intrinsic flattening, the orientation in the top-left panel is such that its symmetry long-axis is along the  $z$ -axis whereas in the remaining panels it is along the  $x$ -axis. Finally, all curves are for a Sérsic profile with index  $n = 2$ , but we have seen before that there is little variation with  $n$ .

## 5. APPLICATIONS AND LIMITATIONS

### 5.1. Inclination Estimates for Individual Galaxies

For individual galaxies a best-effort inclination estimate makes use of the measured projected axis ratio  $b'/a'$  as well as prior statistical or specific (i.e., from kinematics) knowledge about its intrinsic shape.

We first obtain the probability  $f(\vartheta, \varphi | \varepsilon)$  of viewing the galaxy at angles  $(\vartheta, \varphi)$  given its observed ellipticity  $\varepsilon \equiv 1 - b'/a'$ . Then we combine the intrinsic shape and viewing angle distribution by drawing from  $f(p, q)$  and  $f(\vartheta, \varphi | \varepsilon)$  and compute the corresponding distribution of ratios  $r_{\text{med}}/a'$ . For this we need to perform a straightforward one-dimensional numerical integral for any given intrinsic (triaxial) shape distribution  $f(p, q)$ :

$$f(\vartheta, \varphi | \varepsilon) = \frac{\varepsilon(1-\varepsilon)(2-\varepsilon)}{\cos^2 \varphi \sin \varphi} \int_0^1 \frac{f(p, q) \alpha^4}{p q \sqrt{D}} d\alpha^2, \quad (19)$$

where  $\alpha \equiv a'/a$  and

$$D \equiv \varepsilon^2(2-\varepsilon)^2 \alpha^4 \\ - 4 \tan^2 \varphi \cos^2 \vartheta (1-\alpha^2)[1-\alpha^2(1-\varepsilon)^2]. \quad (20)$$

Finally, we combine the distribution in  $r_{\text{med}}/a'$  with the observed  $a'$  including measurement uncertainties to derive  $r_{\text{med}}$ , or more precisely the distribution  $f(r_{\text{med}}|a', b')$ .

We note that shape and size are likely correlated, introducing another level of complexity: in that case the assumption adopted by, e.g., Chang et al. (2013) and van der Wel et al. (2014b) of random viewing angles – independent of measured size or axis ratio – no longer holds. Zhang et al. (2019) examine the implications for the reconstruction of the intrinsic shapes of galaxy populations based on projected shape *and* size distributions (building to a large extent on the work we present now in this paper). They find that for mixed populations of prolate-like and oblate-like systems it is indeed important to do this analysis jointly.

### 5.2. Size Estimates for Individual Galaxies

A broad application of our work is to determine which (projected) size measurement is the best proxy for the physically meaningful  $r_{\text{med}}$ . Traditionally, the circularized effective radius ( $\sqrt{a'b'} = R_e$ , in our notation) has been widely used, while others use  $a'$ , the semi-major axis of the ellipse that encloses 50% of the total light. Using our knowledge of the intrinsic shape distribution of galaxies, we demonstrate here the differences between these approaches, and their sensitivity to intrinsic shape variations and viewing angle distributions.

Chang et al. (2013) and van der Wel et al. (2014b) show that most galaxies in the present-day universe have highly-flattened, nearly oblate geometries. Crucially, this shape distribution generally applies to different types of galaxies: star-forming, quiescent, early-type, late-type, with the exception of galaxies of very low and very high mass (see below). We generate two simulated populations of such oblate and near-oblate objects seen at random viewing angles.

First, representing L\* early-type galaxies (fast rotators), we assume a perfectly oblate population with intrinsic short-to-long axis ratios  $q = 0.3 \pm 0.1$  (Chang et al. 2013), where the error bar reflects the galaxy-to-galaxy Gaussian scatter. The projected size distribution, relative to  $r_{\text{med}}$  is shown in Figure 4 (top left). The major axis radius  $a'$  reproduces  $r_{\text{med}}$  very closely, regardless of viewing angle, while  $R_e$  strongly depends on viewing angle, inducing a large scatter. The median offset is just 18%, but a factor of 2 difference is not a rare occurrence.

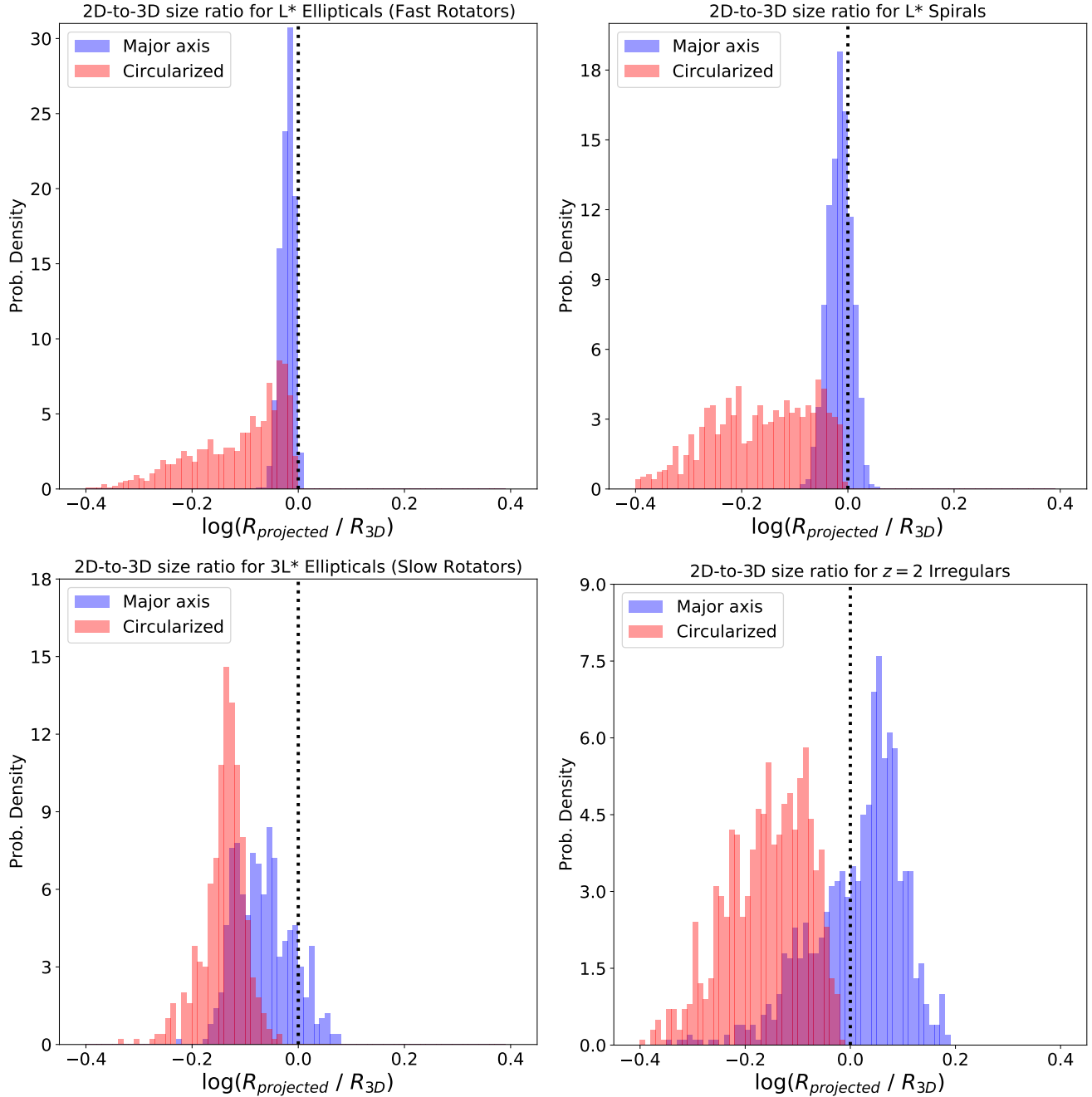


**Figure 4.** Simulated distributions (1000 objects each) of projected-2D to intrinsic-3D size ratios for four different galaxy types. The intrinsic shape distributions of the four types are given in Table 1. The blue histograms represent projected major axis sizes ( $a'$ ) compared to intrinsic median sizes ( $r_{\text{med}}$ ), and red histograms show circularized sizes ( $R_e$ ).

Second, representing  $L^*$  late-type galaxies (spirals), we assume a near-oblate shape distribution with  $q = 0.24 \pm 0.10$  and mild triaxiality  $T = 0.20 \pm 0.10$  to reflect the fact that most spirals are not perfectly circular when viewed face on. Figure 4 (top right) shows similar distributions as for  $L^*$  early-type galaxies, but with a much smaller median value for  $R_e$ :  $R_e/r_{\text{med}} = 0.59$ . For the early types we see a slight offset from unity for  $a'/r_{\text{med}}$ , which is partially due to the lack of any triaxiality and partially due to a higher assumed Sérsic index ( $n = 4$  compared to  $n = 1$ ). The fraction of light projected into a cylinder

compared to the light enclosed within a sphere is slightly smaller for high  $n$  galaxies, but the difference here is just 2%. Of course, for other apertures, e.g., enclosing 20% or 80% of the light these differences are much larger.

It is intuitively obvious that the measured semi-major axis of a disk is invariant with inclination. Therefore, let us consider two classes of galaxies with very different shapes. First, massive ellipticals have been shown to be strongly triaxial. According to Chang et al. (2013) massive ellipticals have a triaxiality of  $T = 0.64 \pm 0.08$  and intrinsic short-to-long axis ratio of  $q = 0.59 \pm 0.18$  (see

**Table 1**  
Projected to intrinsic galaxy sizes for different populations

Population	$T$	$q$	$R_e/r_{\text{med}}$	$a'/r_{\text{med}}$
L* E	0	$0.30 \pm 0.10$	$0.82^{+14\%}_{-25\%}$	$0.96^{+3\%}_{-3\%}$
L* S	$0.20 \pm 0.10$	$0.24 \pm 0.10$	$0.69^{+28\%}_{-23\%}$	$0.97^{+5\%}_{-5\%}$
3L* E	$0.64 \pm 0.08$	$0.59 \pm 0.18$	$0.73^{+7\%}_{-9\%}$	$0.85^{+15\%}_{-11\%}$
$z = 2$ Irr	$0.75 \pm 0.15$	$0.24 \pm 0.10$	$0.71^{+18\%}_{-19\%}$	$1.08^{+13\%}_{-23\%}$

**Note.** — Conversion factors from projected to intrinsic sizes for four galaxy populations: L\* early-type galaxies (Fast Rotators), L\* spiral galaxies, massive elliptical galaxies (Slow Rotators), and low-mass irregular galaxies at redshift  $z = 2$ . Each galaxy population has a different intrinsic shape distribution as indicated by triaxiality  $T$  (see Eq. 2) and short-to-long axis ratio  $q$  with error bars representing the intrinsic (Gaussian) scatter. The median size ratios compare measured projected sizes (circularized  $R_e$  or semi-major axis  $a'$ ) to intrinsic size (median radius  $r_{\text{med}}$ ) with errors reflecting the 16th to 84th percentiles due to random variations in viewing angles and intrinsic shape.

also Vincent & Ryden 2005). For a simulated population of such objects seen at random viewing angles we find medians of  $a'/r_{\text{med}} = 0.85$  and  $R_e/r_{\text{med}} = 0.73$  (see Figure 4, bottom left). Perhaps surprisingly, even for massive ellipticals  $a'$  provides a more accurate estimate of  $r_{\text{med}}$  than  $R_e$ . At the same time,  $R_e$  is more precise in the sense that the scatter in  $R_e/r_{\text{med}}$  is smaller.

Second, high-redshift, low-mass star-forming galaxies, among observed galaxy populations, deviate the most from oblate shapes and therefore provide the most stringent test of our approach. Initiated by the discovery of so-called chain galaxies (Cowie et al. 1995), we have learned that low-mass galaxies at  $z \gtrsim 2$  have very diverse geometries, ranging from oblate to prolate (Ravindranath et al. 2006; Yuma et al. 2012; Law et al. 2012; van der Wel et al. 2014b). Adopting  $T = 0.75 \pm 0.15$  and  $q = 0.24 \pm 0.10$ , we find  $a'/r_{\text{med}} = 1.08$  and  $R_e/r_{\text{med}} = 0.71$  (see Figure 4, bottom right). Once again,  $a'$  provides a less biased galaxy size, and the scatter is similar for  $R_e$  and  $a'$ .

The overall conclusions we draw from this exercise are not as clear-cut as one would like. The decision to use  $a'$  or  $R_e$  depends on the situation. If the sample of relevance has a narrow range in triaxiality  $T$ , then using  $a'$  is preferable because of the lack of bias and small scatter with respect to  $r_{\text{med}}$ . The range in oblateness does not affect this decision: the size distribution of a mix of very thick disks (even spheres) and thin disks is still much better described by  $a'$  than  $R_e$ . If, on the other hand, the sample spans a wide range of triaxialities – or if the triaxiality is unknown – then using  $R_e$  is preferable because of the known, but relatively stable bias. The galaxy-to-galaxy scatter in size is larger in this case, but this is unavoidable in the first place due to the lack of knowledge of the intrinsic shapes.

As a closing remark, let us stress that we explicitly assumed that galaxies are transparent. The effects of viewing-angle dependent extinction is likely the main uncertainty in determining the light-weighted  $r_{\text{med}}$ . Furthermore, one would like to measure mass-weighted sizes instead of light-weighted sizes. Mass-to-light ratio gradients due to age and metallicity gradients can have a large

effect, with mass-weighted projected sizes that are typically 0.2 dex smaller than light-weighted sizes, to first order independent of galaxy type (e.g., Szomoru et al. 2012; Mosleh et al. 2017; Suess et al. 2019). Ideally, stellar surface mass density maps are used in combination with the methodology developed in this paper to arrive at size estimates that can directly be compared with theoretical models and the results from numerical simulations.

Finally, the numerical implementation of the methods presented here can be made available upon request.

We thank the referee for helpful suggestions. This project has received funding from the European Research Council (ERC) under the European Union’s Horizon 2020 research and innovation programme under grant agreement No 724857 (Consolidator Grant ArcheoDyn) and No 683184 (Consolidator Grant LEGA-C).

## REFERENCES

- Baes, M., & van Hese, E. 2011, *A&A*, 534, A69  
 Bezanson, R., van Dokkum, P. G., Tal, T., et al. 2009, *ApJ*, 697, 1290  
 Chang, Y.-Y., van der Wel, A., Rix, H.-W., et al. 2013, *ApJ*, 773, 149  
 Ciotti, L., & Bertin, G. 1999, *A&A*, 352, 447  
 Cowie, L. L., Hu, E. M., & Songaila, A. 1995, *AJ*, 110, 1576  
 de Zeeuw, T., & Franx, M. 1989, *ApJ*, 343, 617  
 Djorgovski, S., & Davis, M. 1987, *ApJ*, 313, 59  
 Dressler, A., Lynden-Bell, D., Burstein, D., et al. 1987, *ApJ*, 313, 42  
 Franx, M. 1988, *MNRAS*, 231, 285  
 Genel, S., Nelson, D., Pillepich, A., et al. 2018, *MNRAS*, 474, 3976  
 Kormendy, J. 1977, *ApJ*, 218, 333  
 Law, D. R., Steidel, C. C., Shapley, A. E., et al. 2012, *ApJ*, 745, 85  
 Ludlow, A. D., Schaye, J., Schaller, M., & Richings, J. 2019, *MNRAS*, 488, L123  
 Mosleh, M., Tacchella, S., Renzini, A., et al. 2017, *ApJ*, 837, 2  
 Mowla, L. A., van Dokkum, P., Brammer, G. B., et al. 2019, *ApJ*, 880, 57  
 Navarro, J. F., & Steinmetz, M. 2000, *ApJ*, 538, 477  
 Parsotan, T., Cochrane, R. K., Hayward, C. C., et al. 2021, *MNRAS*, 501, 1591  
 Prugniel, P., & Simien, F. 1997, *A&A*, 321, 111  
 Ravindranath, S., Giavalisco, M., Ferguson, H. C., et al. 2006, *ApJ*, 652, 963  
 Sersic, J. L. 1968, *Atlas de galaxias australes*  
 Suess, K. A., Kriek, M., Price, S. H., & Barro, G. 2019, *ApJ*, 885, L22  
 Szomoru, D., Franx, M., & van Dokkum, P. G. 2012, *ApJ*, 749, 121  
 Trujillo, I., Rudnick, G., Rix, H.-W., et al. 2004, *ApJ*, 604, 521  
 van der Wel, A., Franx, M., van Dokkum, P. G., et al. 2014a, *ApJ*, 788, 28  
 van der Wel, A., Chang, Y.-Y., Bell, E. F., et al. 2014b, *ApJ*, 792, L6  
 Vincent, R. A., & Ryden, B. S. 2005, *ApJ*, 623, 137  
 Yuma, S., Ohta, K., & Yabe, K. 2012, *ApJ*, 761, 19  
 Zhang, H., Primack, J. R., Faber, S. M., et al. 2019, *MNRAS*, 484, 5170